Geomorphology 512 (2026) 110479

Contents lists available at ScienceDirect

Geomorphology

journal homepage: www.journals.elsevier.com/geomorphology

Deep-seated landslides in tectonically active areas: insights from InSAR data and field evidence in the western Gulf of Corinth (Greece)☆

Francesco Seitone [a,*], Michele Licata [a], Konstantinos Tsanakas [b], Efthimios Karymbalis [b], Giandomenico Fubelli [a]

[a] Department of Earth Sciences, University of Turin, Italy
[b] Department of Geography, Harokopio University of Athens, Greece

ARTICLE INFO

Keywords:
Deep-seated landslides
InSAR
EGMS
Time-series clustering
Corinth Rift
Natural hazard

ABSTRACT

Mapping landslides in tectonically active regions using remote sensing is particularly uncertain where detailed geomorphological constraints are lacking, as measured ground displacements may reflect uplift, subsidence, active faulting, or other deformation processes rather than gravitational slope failure. However, when integrated with field-based geomorphological analysis, remote sensing provides a robust framework for disentangling complex deformation signals. This study investigates deep-seated landslides in a seismically active area 15 km east of Nafpaktos, within the western Gulf of Corinth (Greece), aiming to identify active gravitational processes and quantify their kinematic response to external forcing. A time-series clustering approach was applied to Sentinel-1 InSAR data (2019–2023) to classify ground displacement patterns based on their temporal evolution. Time series from the European Ground Motion Service (EGMS) Ortho product were partitioned to distinguish landslide-related motion from transient deformation associated with seismic activity and other non-gravitational processes. Five landslide sectors were identified and mapped through detailed geomorphological field surveys, allowing the reconstruction of their spatial distribution and temporal evolution. Landslide dynamics were analyzed using descending-orbit time series in relation to rainfall and seismic activity. Comparison of pre- and post-seismic periods reveals a heterogeneous kinematic response: the largest seismic sequence (late 2020–early 2021) did not produce uniform acceleration patterns, but instead modulated slope behavior in a strongly site-specific manner. Rainfall emerges as the primary driver of long-term post-failure displacement in deep-seated landslides, while seismic shaking induces localized, delayed, and prolonged acceleration phases, reflecting time-lagged responses controlled by structural and hydrogeological conditions.

1. Introduction

Understanding and assessing the dynamics of deep-seated landslides in tectonically active regions is essential for defining effective risk mitigation strategies, yet significant challenges remain (Toločka, 2025). Large shallow earthquakes can trigger widespread first-time failures that severely impact infrastructure and influence the long-term evolution of unstable slopes (Keefer, 2002; Bontemps et al., 2020; Mavroulis et al., 2025). Coseismic triggering is mainly associated with dynamic loading induced by ground shaking, which increases shear stress along failure planes and may locally exceed the shear strength of the involved geological materials (Newmark, 1965; Lacroix et al., 2014). Furthermore, the post-failure evolution of landslides is controlled by multiple factors, including low-magnitude seismic activity (Martino et al., 2022). While earthquake-induced first-time failures generally affect jointed rock masses and manifest as disrupted landslides such as rockfalls, topples, or block slides (Keefer, 1984), earthquake-reactivated landslides commonly involve more coherent soils or debris (Martino, 2016). However, earthquake-landslide triggered susceptibility assessment is still challenging especially in the data-scarce regions, also showing particular geoseismic features (intermediate-depth focal characteristics) and transboundary effects of its seismic events (Micu et al., 2023).

Long-term seismic effects that reactivate unstable slopes without causing complete failure are frequently overlooked because they produce subtle deformation rather than catastrophic collapse (Song et al., 2022). Deep-seated landslides often exhibit slow kinematics, ranging

☆ This article is part of a special issue entitled: 'Dynamic Landscapes' published in Geomorphology.

* Corresponding author.
E-mail address: francesco.seitone@unito.it (F. Seitone).

https://doi.org/10.1016/j.geomorph.2026.110479
Received 10 April 2026; Received in revised form 31 July 2026; Accepted 31 July 2026
Available online 3 August 2026
0169-555X/© 2026 The Authors. Published by Elsevier B.V. This is an open access article under the CC BY license (http://creativecommons.org/licenses/by/4.0/).

from millimeters to several centimeters per year, which may persist for months or decades after seismic shaking ceases (Lacroix et al., 2014). In addition, rainfall and seismic shaking may act together in maintaining unstable slopes under critical conditions for prolonged periods. Even low-magnitude earthquakes ($M_w < 4.5$) can modify the kinematic behavior of slow-moving landslides when coupled with persistent precipitation (Bontemps et al., 2020).

From a geological perspective, tectonics control landslide occurrence both passively, through structural weaknesses such as joints, faults, and foliation, and actively, through uplift and vertical movements that increase slope gradients (Carlini et al., 2016). Landslides may therefore develop through the reactivation of pre-existing discontinuities, forming detachment surfaces characterized by residual or sub-peak strength or composite failure surfaces (Jaboyedoff and Labiouse, 2011).

Recent advances in remote sensing and image processing have made satellite, airborne, and terrestrial observations essential for studying earthquake-induced landslides, facilitating the rapid characterization of co-and post-seismic displacements and improving the differentiation between seismic and rainfall forcing to support more reliable multi-hazard scenarios (Micu et al., 2023). Specifically, Interferometric Synthetic Aperture Radar (InSAR) techniques have become fundamental tools for mapping and monitoring large slope movements (Bianchini et al., 2013; Notti et al., 2014; Piacentini et al., 2015; Mantovani et al., 2016; Intrieri et al., 2017; Lakhote et al., 2025). Nevertheless, in tectonically active regions, ground deformation related to uplift, subsidence, or fault activity can obscure landslide-induced motion in Persistent Scatterer (PS) datasets, complicating the interpretation of deformation signals (Lacroix et al., 2022). To improve the interpretation of InSAR products, clustering algorithms have been implemented to categorize PS based on their temporal behavior rather than displacement magnitude. Festa et al. (2023) employed Principal Component Analysis (PCA) for dimensionality reduction and pattern extraction prior to clustering, whereas Poggi et al. (2025) used PCA to identify the dominant spatial and temporal deformation patterns of a large landslide. Rygus et al. (2023) applied Uniform Manifold Approximation and Projection (UMAP), subsequently combining it with clustering algorithms such as k-means and HDBSCAN. Despite these advances, unsupervised clustering results remain sensitive to parameter selection and still

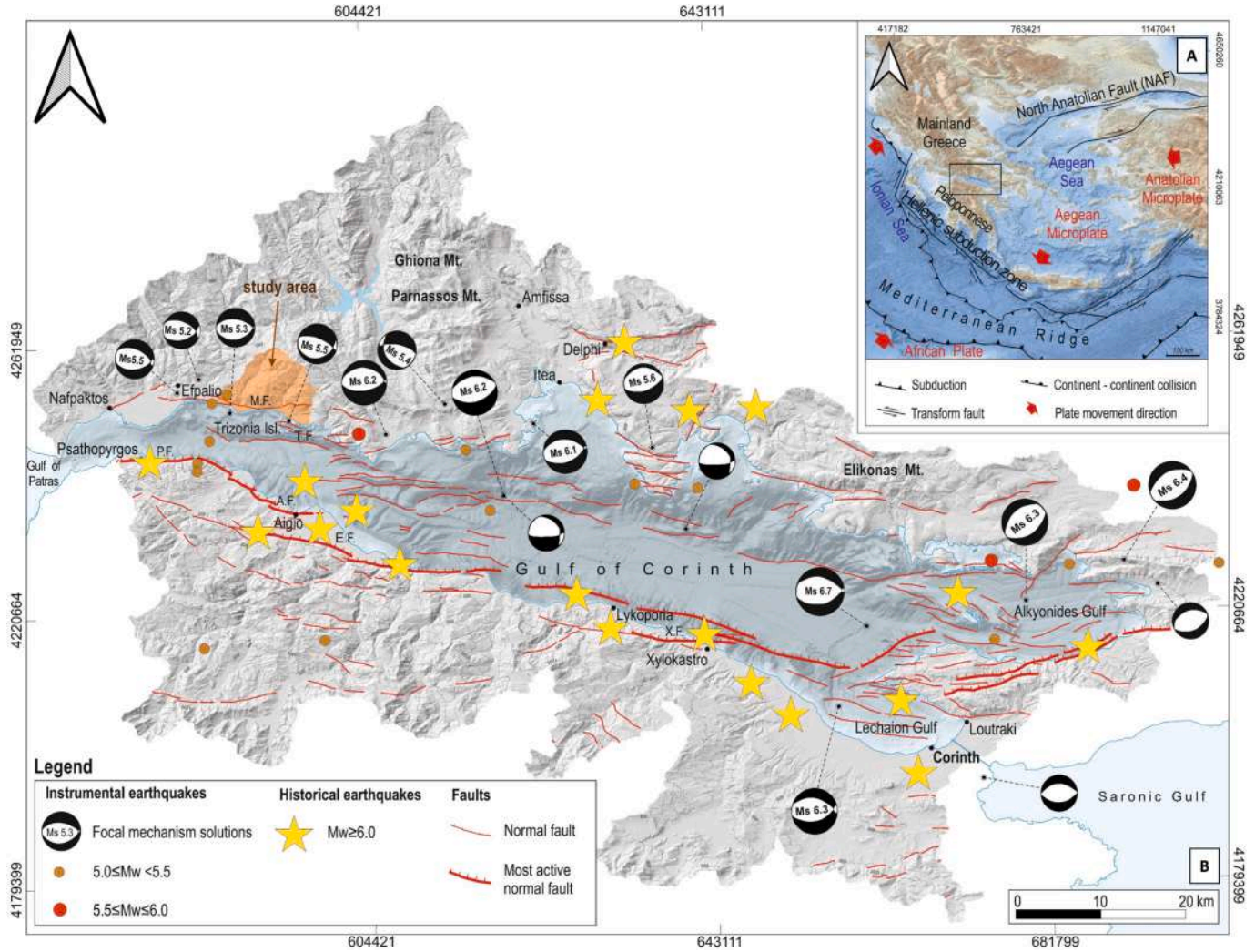

Fig. 1. A) geographical location of the study area; B) Tectonic map of the Gulf of Corinth showing the distribution of active faults across the rift. The map also includes instrumental earthquake epicenters and focal-mechanism solutions. The hillshaded area represents the catchments of the drainage networks draining into the Gulf of Corinth. Active faults are compiled, reassessed, and remapped from previous studies following Fernández-Blanco et al. (2019), with fault selection, remapping, and hierarchy based on Holocene activity. Focal mechanisms of earthquakes with $M_w > 5$ since 1965 are also shown scaled by magnitude (Taymaz et al., 1991; Rigo et al., 1996; Taylor et al., 2011; Lambotte et al., 2014). Shaded relief is derived from a 25 m resolution DEM, resampled from a 5 m Hellenic Cadastre DEM and harmonized with a 25 m resolution bathymetric dataset of the Gulf seafloor (Nomikou et al., 2011). The location of the study area in western-central Greece is also indicated. P.F.: Psathopyrgos fault; A.F.: Aigion fault, E.F.: Eliki fault, and X.F.: Xylokastro fault, M.F.: Marathias fault, T.F.: Trizonia fault. Inset map shows the main geotectonic framework of the broader Aegean region and tectonic setting of the Gulf of Corinth.

require geomorphological constraints for reliable interpretation of landslide activity (Li et al., 2023; Torre et al., 2024).

This study investigates the kinematic behavior of deep-seated landslides in western-central Greece (Fig. 1A). In this context, deep-seated landslides refer to slow- to very slow-moving slope failures (Varnes, 1978) occurring in rock masses with rupture surfaces deeper than 5 m, following Parkash (2020) definition. The current research focuses on medium- to large-scale landslides according to the classification proposed by McColl and Cook (2024), excluding Deep-seated Gravitational Slope Deformations (DGSDs), according to the terminology of Soldati (2013).

Although the Gulf of Corinth is one of the most tectonically active regions in Europe, active large-scale deep-seated landslides in its northwestern sector have not yet been systematically investigated through the integration of remote sensing observations and geomorphological field surveys. In addition, deformation signals related to tectonic activity, subsidence, and slope processes may overlap spatially and temporally, complicating the identification of gravitational deformation through InSAR series.

To address these limitations, Sentinel-1 displacement data were analyzed using a k-means time-series clustering approach integrated with detailed field investigations. The time-series clustering was specifically adopted to distinguish slope-related deformation from ground motion potentially associated with fault activity and subsidence, reducing ambiguities in multi-source deformation environments. Following the identification of active landslide sectors, displacement trends were analyzed in relation to rainfall and seismic activity recorded between 2019 and 2023, including five earthquakes with moment magnitudes ranging from 4.5 to 5.2 M_w (Kaviris et al., 2021), to evaluate the relative influence of hydro-meteorological and seismic forcing on landslide kinematics.

2. Study area

The study site is located along the northern margin of the western Gulf of Corinth (Greece), approximately 15 km east of Nafpaktos, north of the island of Trizonia, roughly 20 km northeast of the Rion–Antirion Bridge. In Fig. 1B, the study area is highlighted with an orange polygon. The investigated sector covers ~81 km^2, extending from sea level up to the watershed, whose highest point reaches 1548 m a.s.l., with an average elevation of about 652 m a.s.l.

2.1. Geological setting

The Gulf of Corinth is a WNW–ESE trending active amagmatic continental rift (Doutsos and Piper, 1990; Armijo et al., 1996; Fernández-Blanco et al., 2019) separating mainland Greece from the Peloponnese and cross-cutting the older Hellenides fold-and-thrust belt (Fig. 1B). It constitutes one of the fastest-extending continental rifts and one of the most seismically active tectonic regions in Europe (Armijo et al., 1996; Bernard et al., 2006). Geotectonically, the Gulf of Corinth lies northeast of the Hellenic subduction trench, southwest of the western termination zone of the North Anatolian Fault, and within the actively extending Aegean domain. This tectonic setting places the rift within a complex stress field controlled by both southward rollback of the African slab and the westward propagation of Anatolian escape tectonics (Armijo et al., 1999; Reilinger et al., 2009). The Corinth Rift initiated during the late Miocene as part of the back-arc extensional regime associated with subduction of the African plate beneath the Aegean microplate. Slab rollback promoted crustal extension and thinning, leading to the formation and progressive evolution of the rift. More broadly, the Corinth rift records the tectonic evolution of the Aegean region from post-orogenic distributed extension following collapse of the Hellenic orogen to localized Quaternary rifting. As one of the most evolved segments of this extensional system, the Gulf of Corinth currently accommodates rapid N—S extension, with geodetic measurements showing a clear westward increase from <5 mm/yr in the easternmost gulf to ~14–16 mm/yr in the western sector (Briole et al., 2000). The western rift thus represents the most actively deforming part of the system, with extension rates among the highest documented globally (Avallone et al., 2004; Briole et al., 2021; Fernández-Blanco et al., 2019).

The regional tectonic framework of the Gulf of Corinth is summarized in the accompanying tectonic map (Fig. 1B), which compiles published active-fault datasets together with updated structural interpretations (Fernández-Blanco et al., 2019; Rossi et al., 2026). The map illustrates the distribution and segmentation of active faults across the rift system and includes instrumental earthquake epicenters and focal-mechanism solutions, providing an overview of both the structural framework and present-day tectonic activity (Taymaz et al., 1991; Rigo et al., 1996; Taylor et al., 2011; Lambotte et al., 2014). The distribution of earthquake epicenters and focal-mechanism solutions indicates that the rift is currently dominated by normal faulting associated with a regional N—S extensional stress regime, locally accompanied by minor oblique-slip components (Fig. 1B). Structurally, the rift is dominated by an en-echelon system of E–W to WNW–ESE trending normal faults that collectively form a rift-scale fault zone exceeding ~80 km in length (Fernández-Blanco et al., 2019). The rift displays a marked asymmetry, with major north-dipping border faults along the southern margin and steeper south-dipping antithetic faults along the northern margin (Kaviris et al., 2021). The major faults along the southern margin (from west to east) include the Psathopyrgos fault, which records relatively low uplift rates of ~0.7–0.8 mm/yr (Houghton et al., 2003), the Aigion fault with rates of ~1.6–2.7 mm/yr (Palyvos et al., 2005; Palyvos et al., 2008), the Eliki fault with uplift rates of up to ~3–5 mm/yr during the Late Pleistocene (McNeil et al., 2005), and the Xylokastro fault, which reaches sustained long-term slip rates of ~6–7 mm/yr (Armijo et al., 1996), highlighting pronounced spatial variations in deformation intensity across the rift system. These variations in fault activity reflect the overall structural asymmetry of the rift and its along-strike segmentation. The northwestern margin is defined by the Marathias and Trizonia faults, which exhibit relatively low average Late Quaternary slip rates of ~0.36–0.44 mm/yr, reinforcing the contrast in fault activity between rift margins (Beckers et al., 2015; Kaviris et al., 2022).

Seismicity is concentrated mainly in the central and western sectors of the Gulf of Corinth, where it broadly coincides with the mapped fault network (Fig. 1). This pattern indicates that these sectors represent the most active parts of the rift and are characterized by frequent shallow crustal earthquakes (Makropoulos et al., 2012; Zahradník et al., 2022). The most recent $M_w > 6$ event was the 1995 M_s 6.2 Aigion earthquake (Bernard et al., 1997). Since 2010, several earthquakes with $M_w \geq 5$ have occurred, including the January 2010 M_w 5.2–5.3 Efpalio doublet (Sokos et al., 2012), the November 2014 M_w 5 (Kaviris et al., 2018), and the March 2019 M_w 5.1 earthquakes. Between December 2020 and February 2021, the western Gulf of Corinth experienced a seismic crisis that began with an M_w 4.6 earthquake near the northern shore, opposite Aigion, followed by an M_w 5 event that marked an eastward migration of activity toward Trizonia Island. The sequence culminated with an M_w 5.3 earthquake approximately 3 km northeast of the Psathopyrgos fault (Kaviris et al., 2021).

The study area comprises geological formations of the Olonos-Pindos geotectonic unit, one of the most characteristic nappes of the Hellenides, distinguished by its well-developed pelagic stratigraphic sequence (Papanikolaou, 2021). It belongs to the external Hellenides domain, and its sedimentary record reflects the progressive closure of the Pindos–Cyclades oceanic basin, during which deep-sea sediments were detached and emplaced onto the adjacent carbonate platform. The study area is composed of deep-water carbonate, siliciclastic, and siliceous sedimentary rocks of Jurassic to Eocene age (Tsoflias and Loftus, 1971; Paraschoudis, 1977). Specifically, they include fine-grained, reddish to white limestones of Jurassic age, locally oollithic in texture and interbedded with red shales and cherts (Fig. 2).

Overlying these are cherts and limestone of Lower to Upper

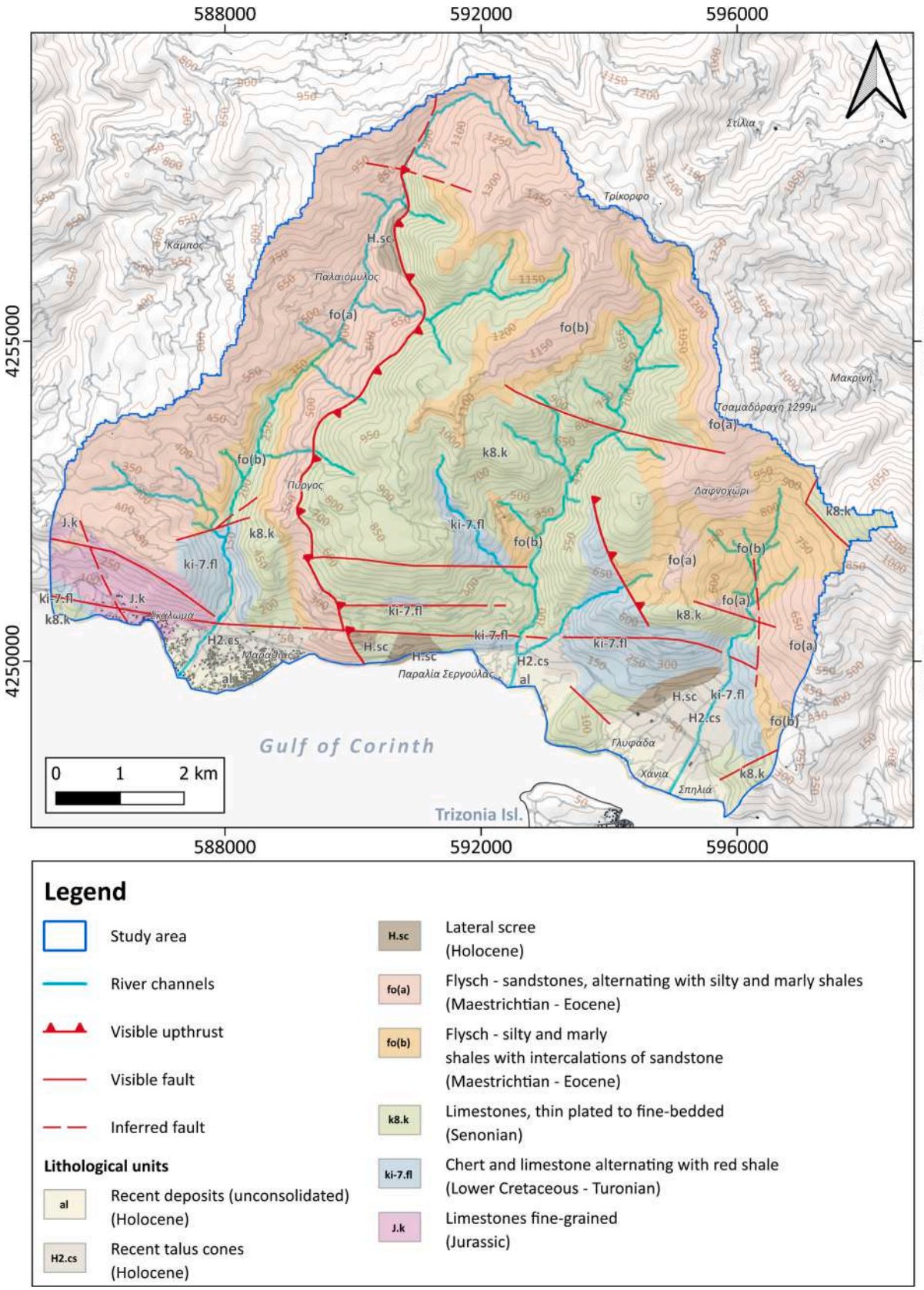

Legend

- Study area
- River channels
- Visible upthrust
- Visible fault
- Inferred fault

Lithological units

- al — Recent deposits (unconsolidated) (Holocene)
- H2.cs — Recent talus cones (Holocene)
- H.sc — Lateral scree (Holocene)
- fo(a) — Flysch - sandstones, alternating with silty and marly shales (Maestrichtian - Eocene)
- fo(b) — Flysch - silty and marly shales with intercalations of sandstone (Maestrichtian - Eocene)
- k8.k — Limestones, thin plated to fine-bedded (Senonian)
- ki-7.fl — Chert and limestone alternating with red shale (Lower Cretaceous - Turonian)
- J.k — Limestones fine-grained (Jurassic)

Fig. 2. Geological map of the study area based on the 1:50,000 scale geological maps produced by the Institute of Geology and Mineral Exploration of Greece (IGME) (Tsoflias and Loftus, 1971; Paraschoudis, 1977).

Cretaceous age, alternating with red shales. In the lower sections, red cherts with intercalations of argillaceous shales and marls dominate, whereas the upper sections are characterized by polygenic microbrecciated limestones, commonly referred to as first flysch. The succession continues upward with thinly bedded to finely laminated pelagic limestones of Upper Cretaceous age, containing nodules and thin chert layers, which gradually transition into microbrecciated limestones (Fig. 2). Higher in the sequence, flysch formations of Upper Cretaceous to Eocene age appear. The lower transitional members consist of bluish-grey silty and marly shales interbedded with sandstones, which grade upward into sandstones with intercalations of silty shales. The basic structural pattern of the study area was established during the Alpine folding. The rocks of the Olonos-Pindos geotectonic unit are extensively folded and faulted, a result of compressional forces during the Alpine orogeny that created a "fold and thrust belt" (Skourlis and Doutsos, 2003; Athanassas et al., 2021). The rocks are characterized by numerous west-verging folds, including overturned folds and fault-bend folds, as well as thrust faults, which have been reactivated by later extensional and strike-slip faulting, particularly in the Neogene. The study area is cross-cut by the Marathias fault, a WNW-trending structure approximately 17 km in total length, comprising two prominent segments. Geomorphic indicators including stream deflections, drainage capture, and knickpoint development along the fault trace indicate that the Marathias fault is active, with a significant portion of its deformation accommodated during earthquake activity (Gallousi and Koukouvelas, 2007).

2.2. Geomorphological framework

The geomorphology of the Corinth Rift's reflects the strong interaction between active tectonics during the Quaternary, high erosion rates, and depositional processes (Armijo et al., 1996; Fernández-Blanco et al., 2019; Rossi et al., 2026). The landscape is dominated by steep, fault-controlled mountain fronts, particularly along the southern margin, where uplifted footwall blocks form a rugged relief with sharp escarpments and deeply incised valleys. The southern terrestrial sector shows clear evidence of continuous tectonic uplift, such as marine terraces up to approximately 400 m a.s.l., elevated Gilbert-type fan-delta deposits at high elevations (reaching 1756 m a.s.l.), uplifted tidal notches, and reversed drainage features (Fernández-Blanco et al., 2019; Rossi et al., 2026). In contrast, the northern part is notable for the absence of Quaternary marine or lacustrine sediments and displays submerged tidal notches, indicating ongoing tectonic subsidence. However, the northern margin of the western sector records also significant fault segmentation and localized uplift, mainly due to the activity of the Marathias fault zone, which is parallel to the coastline (Zahradník et al., 2022). Drainage networks are steep, and highly responsive to tectonic forcing, often exhibiting knickpoints and incised channels that reflect ongoing base-level changes (Tsanakas et al., 2025). At the mouths of streams, coastal fans have developed through the accumulation of coarse-grained sediments transferred from the high-relief hinterland (Karymbalis et al., 2018).

In the terrestrial sector of the western Corinth Rift, mass movements are frequent. Landslide occurrences provide critical insights into the interaction between active faults and pre-existing structures, facilitated by prominent outcrops, moderate rainfall, and minimal anthropogenic disturbance. Koukis et al. (2009) investigated the landslides triggering mechanisms in the southern Gulf of Corinth, identifying a robust spatial correlation between active normal faults and highly sheared lithological units, such as flysch and Neogene sediments. Their findings indicate that seismic activity and intense or prolonged rainfall events drive slope reactivation, particularly along infrastructure corridors where recurrent failures have required continuous stabilization measures and risk mitigation works. Sabatakakis et al. (2015) documented that the periodic reactivation of the Panagopoula landslide, located southwest of the Gulf of Corinth, is strongly controlled by active faulting and prolonged rainfall. These movements primarily affect tectonically sheared flysch and Neogene sediments, exhibiting persistent instability despite previous mitigation efforts. Moreover, recent spatial-statistical analyses of slope failures and tectonic structures were conducted by Bathrellos et al. (2024) in the northwestern Peloponnese, near Patras (~30 km southwest of this study site). Their results indicate that landslide susceptibility is primarily controlled by lithology, slope angle, and proximity to both tectonic discontinuities and drainage networks. The highest landslide densities occur on steep slopes and within 50–100 m of fault traces and fluvial streams.

Similarly, Gallousi and Koukouvelas (2007) demonstrated that the distribution and occurrence of large landslides throughout the study area (north of the western Gulf of Corinth coastline) is strongly controlled by proximity to tectonic structures, particularly at the intersections of normal and thrust faults. Moreover, through photogrammetric analyses of historical aerial photographs, the authors identified a major coseismic first-failure event in 1969, triggered by a M_w 6.5 earthquake, which occurred within the same area investigated in this study.

3. Materials and methods

3.1. Data sources

Ground displacements in the study area were investigated using satellite-based InSAR data from Sentinel-1, due to the absence of in situ monitoring instruments and the need to cover large spatial extents. Ortho Vertical, Ascending, and Descending (calibrated 2B) datasets were obtained from the European Ground Motion Service (EGMS) for the period 2019–2023 (Crosetto et al., 2020). Sentinel-1 operates in a near-polar, sun-synchronous orbit, providing repeat-pass coverage of the same area approximately every 6 to 12 days. The Ortho Vertical product was used during the remote mapping phase to detect ground movements, while the Ascending and Descending datasets were used to analyze velocity trends and cumulative displacements of the mapped landslides.

Seismic data were obtained from the National Kapodistrian University of Athens (NKUA) Seismological Laboratory, which provides a comprehensive catalog of earthquakes in Greece from June 2018 onward (Fig. 3). Approximately 17,000 earthquakes recorded between 2018 and 2023 within a ~ 35 km radius of the study area center were considered for analysis.

To identify the main seismogenic structures within the study area, the active fault catalog compiled by Fernández-Blanco et al. (2019) was employed. In this catalog, fault selection, remapping, and hierarchical classification are based on evidence of Holocene activity.

In the absence of rain gauge stations near the study area, we used satellite-derived precipitation data from Climate Hazards Group InfraRed Precipitation with Station dataset (CHIRPS; Funk et al., 2015). CHIRPS is a near-global rainfall dataset covering latitudes from 50°S to 50°N since 1981, combining in situ station data, satellite imagery, and climatology to provide high-resolution gridded rainfall time series suitable for trend analysis and drought monitoring. Daily rainfall data from twelve cells (with a spatial resolution of 0.05°, approximately 5 km; Fig. 3) were extracted for 2018–2023 from this large dataset.

Finally, the official 1:50,000-scale geological map of Greece published by the Institute of Geology and Mineral Exploration of Greece (IGME) (Nafpaktos and Amygladea sheets; Tsoflias and Loftus, 1971; Paraschoudis, 1977) was consulted to identify the main lithological units of the study sector.

3.2. Methodological workflow

This study adopts a three-tiered methodological framework (Fig. 4). First, vertical ground-motion time series derived from the InSAR Ortho product were processed using a clustering algorithm to partition the

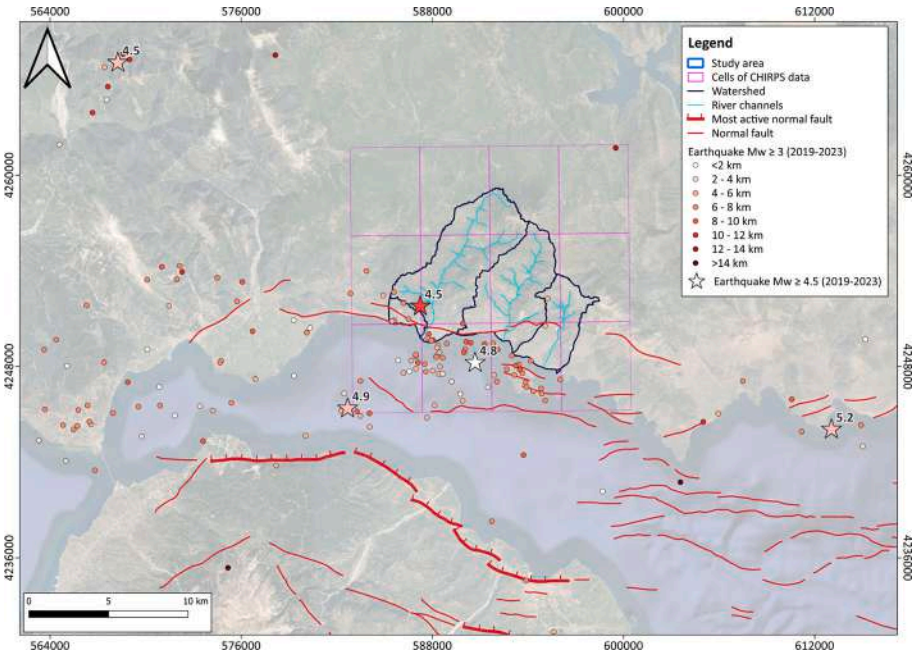

Fig. 3. Spatial distribution of earthquakes from the NKUA dataset (including hypocentral depth), active faults from Fernández-Blanco et al. (2019) dataset, and CHIRPS rainfall data cells. The watershed boundaries of the analyzed basins are also shown. Maximum elevations are 1548 m a.s.l. for the western basin, 1506 m a.s.l. for the central basin, and 1331 m a.s.l. for the eastern basin, whereas the minimum elevation is 0 m a.s.l.

study area based on modal temporal trends (Fig. 4A). This step aims to distinguish landslide-specific displacement styles from background tectonic signals. Second, the clustering results were integrated with geomorphological field surveys to characterize and validate the identified landslide-prone sectors (Fig. 4B). Finally, for each mapped active landslide, we performed a detailed analysis by relating displacement time series to seismic events and daily rainfall data to assess the main controls on slope instability during the study period (Fig. 4C).

The initial phase involved the extraction and preparation of vertical ground deformation time series from the EGMS Ortho dataset for the 2019–2023 observation period. A preliminary filtering was applied to isolate PS exhibiting only negative (downward) displacement rates. The resulting time series were then classified according to their displacement behavior using a k-means clustering algorithm, implemented with a Euclidean distance method. The optimal number of clusters (k) was explored within the range $2 \leq k \leq 20$. Clustering performance was evaluated using three validation indices: the silhouette score (Rousseeuw, 1987), the inertia (MacQueen, 1967) and the Davies–Bouldin index (Davies and Bouldin, 1979).

Field surveys were subsequently conducted in summer 2024 and spring 2025 to validate preliminary remote sensing interpretations. Active landslides and relict gravitational phenomena were mapped using traditional geomorphological methods combined with Unmanned Aerial Vehicle (UAV) surveys.

The specific analysis phase was performed independently for each mapped landslide area (Fig. 4C). Morphometric indices were calculated to evaluate slope exposure relative to the satellite's Line of Sight (LOS), enabling the calculation of the mean sensitivity index. According to van Natijne et al. (2022), this index serves as a priori indicator of the potential efficacy of InSAR-based monitoring, as the effectiveness of such campaigns is highly contingent upon the acquisition geometry and the density of coherent scatterers over the investigated slopes. Based on the sensitivity assessment, ascending-orbit data were excluded due to their extremely low sensitivity to the investigated deformation patterns. These data were filtered to retain only reliable PS by applying a minimum temporal coherence threshold of 0.5 (as suggested by Notti et al., 2014) and a maximum acceptable RMSE of 4.0 mm for the fitted deformation model. LOS velocity time series were derived from the InSAR descending dataset, and results are presented in terms of median velocity and the associated interquartile range (IQR).

To suppress high-frequency noise and mitigate seasonal signal fluctuations, landslide velocity displacement was calculated using a 60-day rolling window. This specific temporal scale was selected to optimize the balance between signal sensitivity and noise reduction, specifically tailored to the regional geodynamic and hydrogeological context. Preliminary tests indicated that a 30-day window was overly sensitive to short-term meteorological noise and failed to account for the hydrogeological time lag inherent in the deep-seated failures in this region (Koukis et al., 2009; Sabatakakis et al., 2015). Conversely, a 90-day window was rejected as it excessively smoothed the kinematic signal, potentially masking discrete reactivation pulses and the sharp transitions of the Mediterranean wet season, thereby weakening the correlation with specific seismic or peak-rainfall events. Accordingly, cumulative rainfall was computed over an identical 60-day window to reflect sustained hydrological loading.

Seismic activity was integrated by quantifying the cumulative number of earthquakes with $M_w \geq 3$ over the same 60-day intervals. This aggregation window is appropriate for the tectonic setting of the study area because it captures seismic swarms and aftershock sequences, which have been identified as key triggers of first-time slope failures (Gallousi and Koukouvelas, 2007; Bathrellos et al., 2024), while avoiding excessive temporal smoothing.

Finally, to identify coherent kinematic patterns with external forcings (seismicity and precipitation) a multiparametric k-means cluster analysis was performed using the GEMMA Toolbox (Pilade et al., 2025). This R-based software is designed for the multi-parametric analysis of large, heterogeneous geoscientific datasets.

4. Results

4.1. Landslides detection

To differentiate diverse geological phenomena using a single deformation vector, we applied a time-series clustering to the vertical EGMS InSAR dataset, specifically targeting PS exhibiting negative (downward) displacement trends. This approach facilitated the identification of three

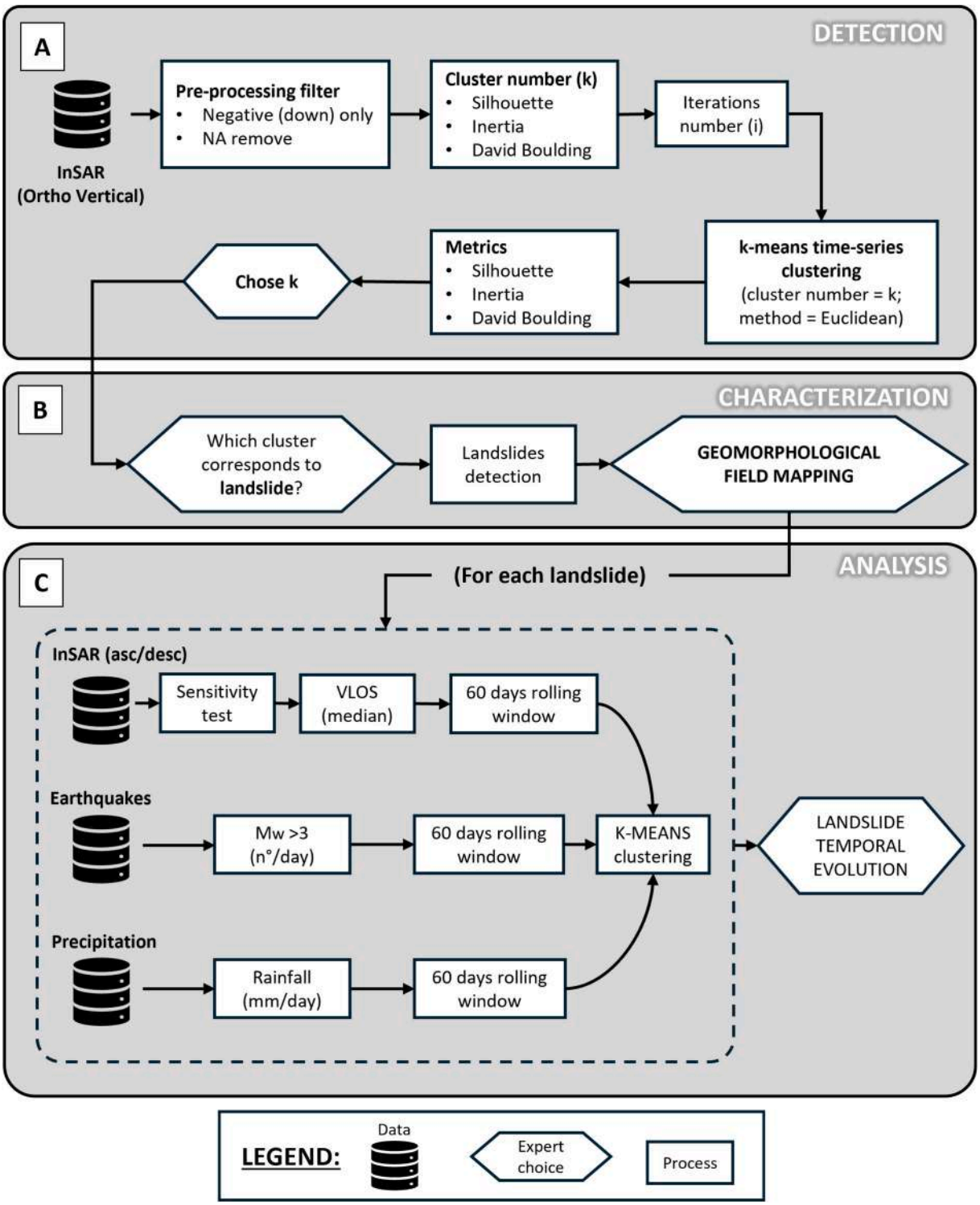

Fig. 4. Methodological workflow employed in this study. A) Semi-automated landslide detection via k-means time-series clustering; B) Field validation and geomorphological characterization; C) Multi-parametric analysis of the kinematic response of individual landslides (VLOS = line of sight velocity) to seismic forcing and precipitation.

distinct kinematic regimes characteristic of the area investigated: slope instability, deltaic-fan subsidence, and normal faulting.

While employing only the vertical component omits the horizontal motion often inherent in landslide kinematics, it provides a distinct advantage when the primary objective is to disentangle tectonic-driven signals from gravitational movements within a cluster-based framework.

Fig. 5A provides statistical information on the PS population analyzed. The distributions of mean velocity and mean acceleration of the series are approximately unimodal and near-Gaussian, with mean values predominantly negative, indicating a general downward vertical motion within the study area. The correlation matrix highlights weak linear relationships between kinematic variables, mean velocity and mean acceleration, and the seasonality amplitude. The low correlation indicates limited redundancy, validating the inclusion of PS

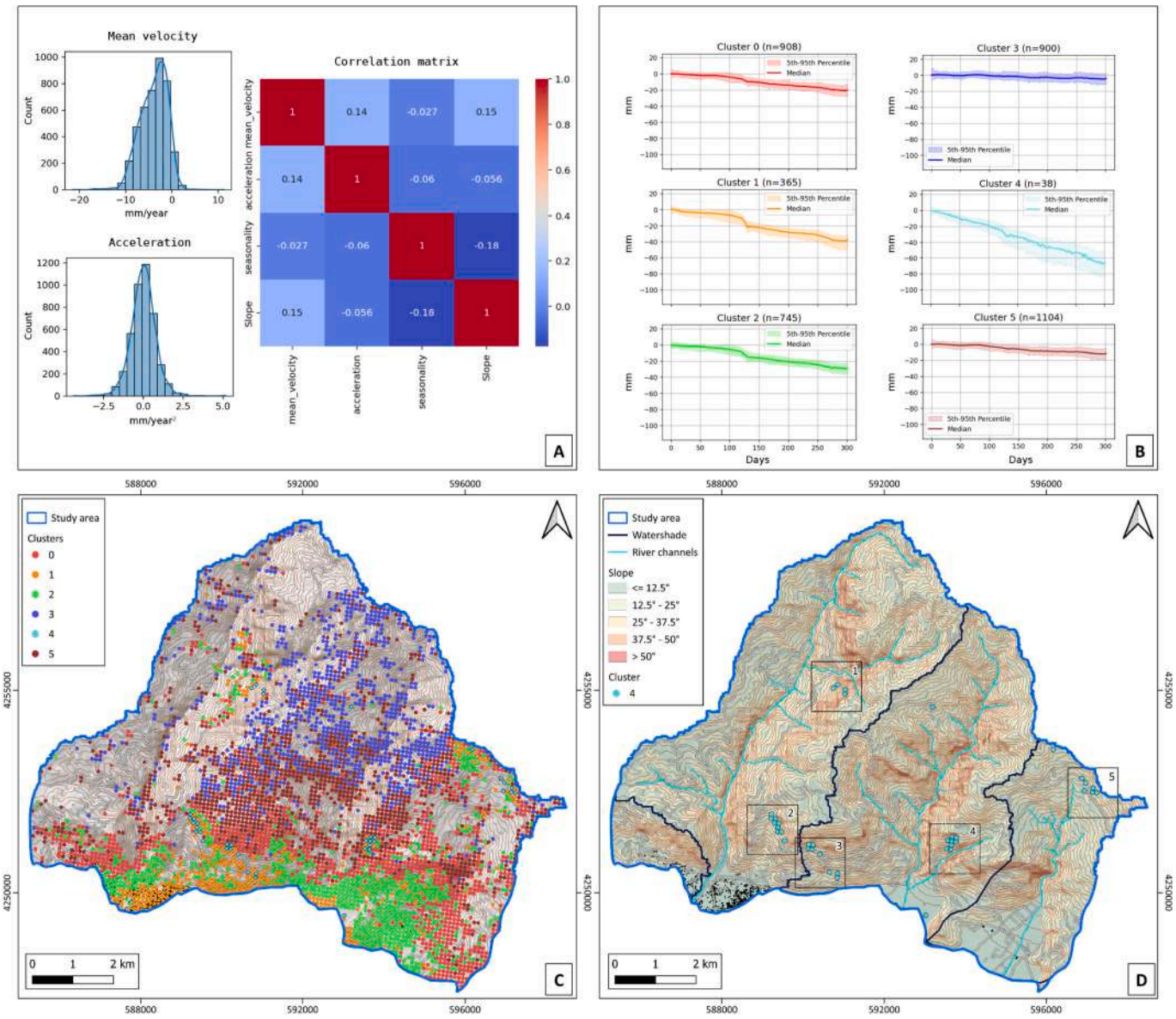

Fig. 5. Results of the time-series clustering analysis applied to vertical Ortho InSAR dataset. A) Exploratory velocity and acceleration data analysis of the full dataset, and correlation matrix; B) Temporal displacement patterns of the six identified clusters, displaying median displacement trends (solid lines) and 5th–95th percentile envelopes (shaded regions); C) Spatial distribution of the clustering result across the study area; D) Geographic delineation of Cluster 4 with inset boxes highlighting the five sectors prioritized during the subsequent field investigation.

displacement data in the clustering procedure.

The time-series cluster analysis reveals six distinct temporal patterns within the InSAR Ortho vertical dataset (Fig. 5B). These clusters exhibit kinematic patterns ranging from relatively stable, subtly deforming trends to progressively accelerating downward trends, reflecting diverse deformation regimes present in the studied area. Cluster 4 is particularly distinct, characterized by continuous movement throughout the five-year observation period. In contrast, Clusters 0, 1, and 2 exhibit a marked, sudden acceleration following an initially stable period. Cluster 3 presents the most stable time series, while Cluster 5 comprises slightly unstable PS with minor negative displacement fluctuation. It is important to note that the EGMS Ortho data used here includes all ground motion components, including potential long-term tectonic contributions, which may influence the interpretation of cluster behaviors. The spatial distribution of these clustering results, reported in Fig. 5C, demonstrated significant spatial coherence rather than random dispersion. Specific kinematic classes are preferentially within the morphological sectors, most notably along slope systems and deltaic-fan areas. Cluster 4 is characterized by persistent downward displacement without periods of quiescence (Fig. 5B), and exhibits a pronounced spatial pattern concentrated within five different slope sectors (Fig. 5D). This cluster is probably linked to the landslide activity. These areas, highlighted by five inset boxes in Fig. 5D, were prioritized for subsequent geomorphological field investigations and detailed ground-truthing.

4.2. Landslides mapping and characterization

The five areas characterized by a high likelihood of active slope deformation (Fig. 5D) were investigated through geomorphological field surveys. Field observations confirmed the presence of five slope movements, primarily classified as large complex deep-seated landslides (Fig. 6A). While their initial triggering mechanisms remain uncertain, their current kinematic behavior is characterized by both episodic reactivations and persistent long-term creep, as revealed by remote sensing data.

Field investigation also revealed several landslide-prone areas where

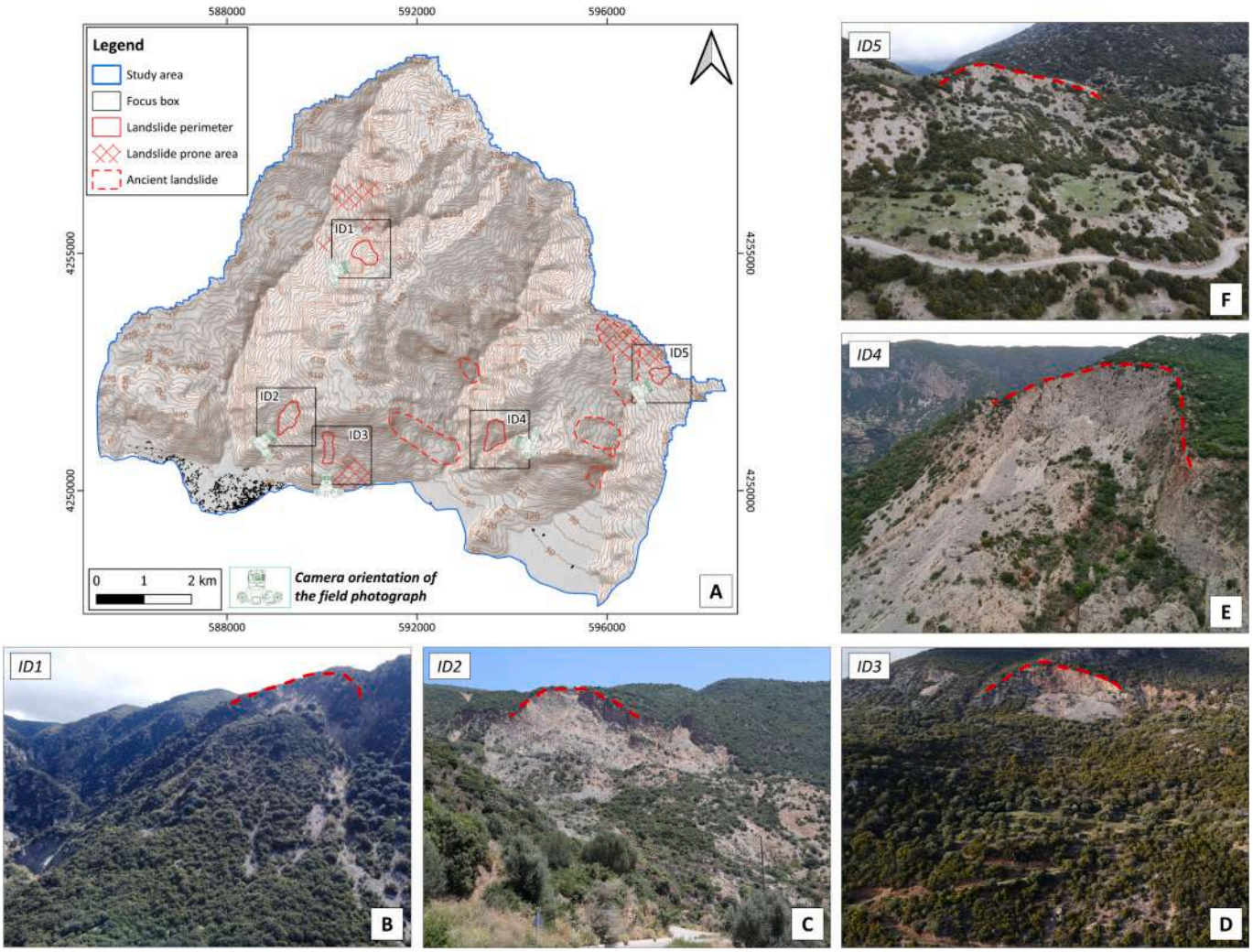

Fig. 6. A) Spatial distribution of landslides identified through the time-series clustering method. Field evidence of the mapped landslides, main crowns (dashed red lines), and associated identification codes: B) landslide ID1; C) landslide ID2; D) landslide ID3; E) landslide ID4; F) landslide ID5.

geomorphological conditions suggest the potential for future failures (Fig. 6A), despite the absence of detectable motion in the InSAR dataset we analyzed. Furthermore, distinct landforms attributable to very large ancient landslides were recognized (Fig. 6A). These relict slope failures appear currently inactive; their primary features are significantly modified by exogenous processes, which have partly obliterated their original geomorphological expression. Also, field photographs acquired over the five active landslide sites clearly highlight the main crowns and the characteristic morphological signatures (Fig. 6B, C, D, F).

Detailed geomorphological maps were produced for each inset area (Fig. 7A, B, C, D, E), highlighting the spatial relationships between landforms and the exposed lithological units. The maps reveal a complex assemblage of gravity-driven processes extending beyond the main landslide bodies. In addition to large landslides, several secondary geomorphological phenomena were mapped, including debris-flow channels and accumulation areas, gully networks, scree slopes, trenches, and mixed erosional–depositional features.

The coexistence of large landslides with smaller-scale gravitational processes suggests a long-term and progressive evolution of slope characterized by reactivations and surface remodeling (Fig. 8A, B). For instance, Fig. 8C illustrates a mixed debris-flow and alluvial deposits accumulation whose channel is located within the body of the landslide ID2. Moreover, field observations provided further evidence of karst-related processes affecting the investigated slopes. Localized carbonate recrystallization and the development of cemented carbonate textures were observed in the landslide's body material (Fig. 8D), likely associated with subsurface water circulation along preferential flow paths. The detailed mapping shows that deep-seated landslide activation frequently occurs in proximity to tectonic structures (Fig. 8E) and along lithological boundaries, particularly at the contact between limestone and siliciclastic units. These structural and lithological controls appear to play a key role in localizing slope instabilities and governing their morphological expression, with the bedrock being locally highly fractured (Fig. 8F).

4.3. Landslides temporal evolution analysis

Following the landslides mapping phase, we evaluated the geometric sensitivity of the Sentinel-1 radar acquisition relative to the investigated landslides. The sensitivity index was computed according to the approaches proposed by van Natijne et al. (2022). Previous studies have suggested that landslides characterized by sensitivity values greater than approximately 0.2 are generally suitable for deformation monitoring using InSAR techniques (Notti et al., 2014). All analyzed landslides in the current research yielded general sensitivity values above this reference threshold, with total sensitivity ranging between 0.27 and 0.81, indicating favorable geometric conditions for Sentinel 1-based monitoring.

Nevertheless, a pronounced discrepancy was observed between the two acquisition geometries (Table 1). Sensitivity values for ascending

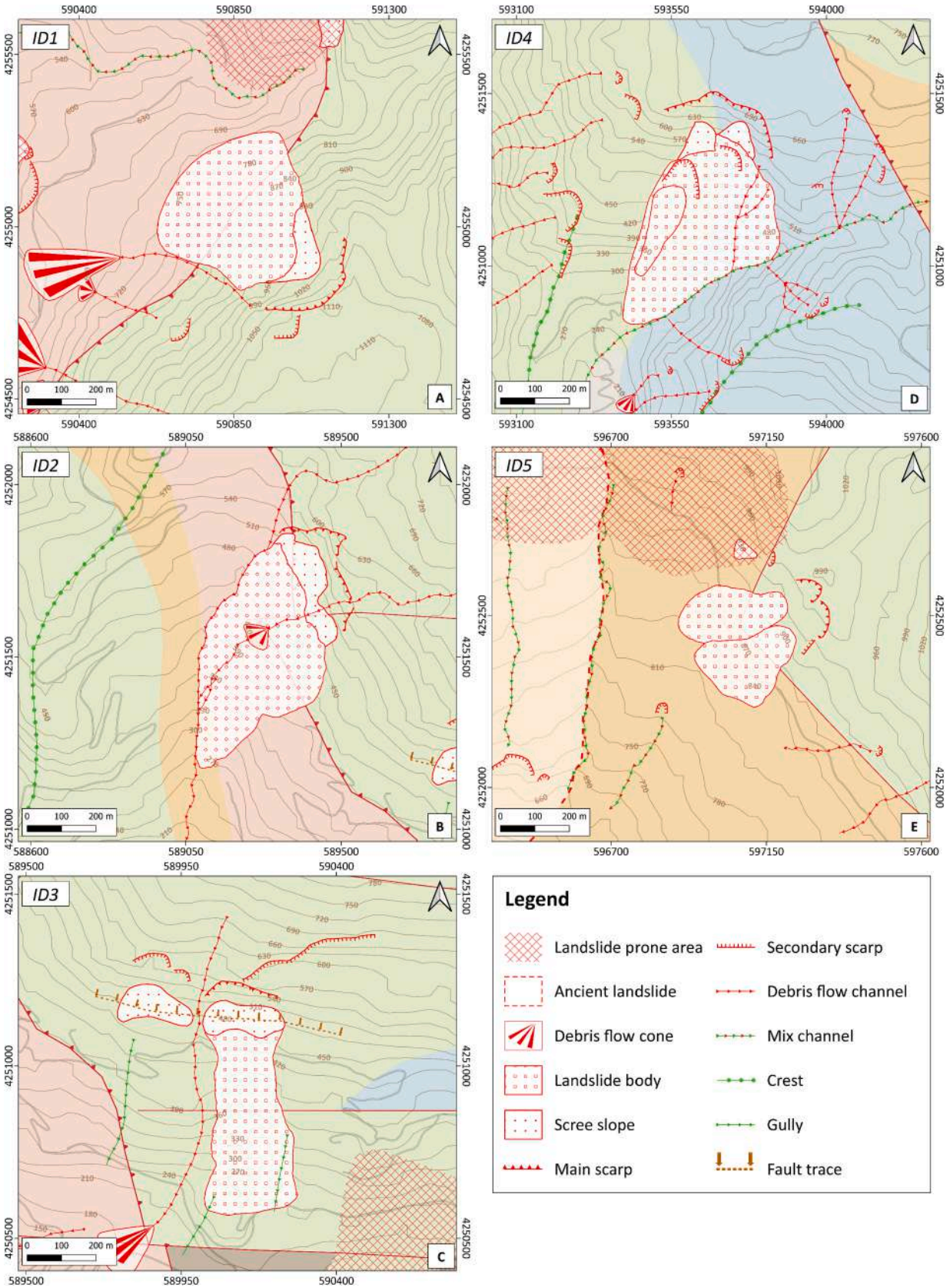

Fig. 7. Geomorphological maps of the five inset boxes: A) landslide ID1; B) landslide ID2; C) landslide ID3; D) landslide ID4; E) landslide ID5. The landslide bodies are lightly transparent to highlight the geological structures shown on the geological map (see Fig. 2 for the geological legend).

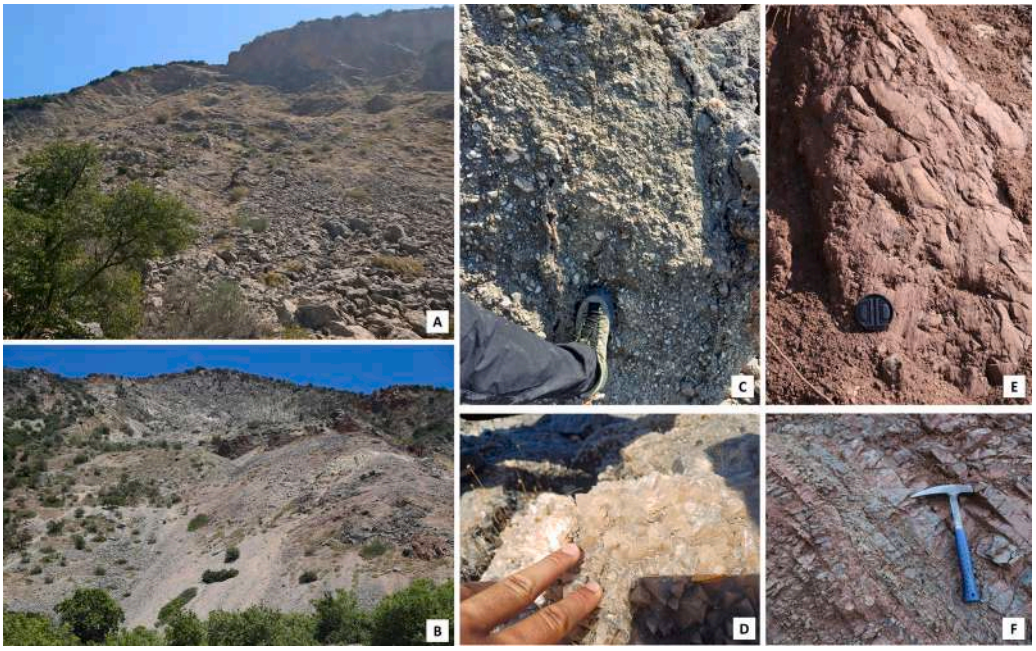

Fig. 8. Photos taken during the field surveys. A) crown area of landslide ID2 in the background, with several decametric blocks visible in the foreground; B) the massive landslide ID4 body characterized by heterogeneous debris deposits containing angular, sharp-edged limestone blocks of variable size, reflecting the fragmented nature of the displaced material; C) accumulation zone consisting of mixed debris-flow and alluvial deposits, highlighting the interaction between gravitational and fluvial processes; D) evidence of recrystallization observed on a displaced block; E) slickenlines along the Marathias active fault system, near the landslides ID2 and ID3; F) fractured limestone alternating with red shale.

Table 1
Landslide areas sensitivity index respect to the Sentinel-1 radar geometry sensors, according to van Natijne et al., 2022, and morphometric metrics. The data in the table reflects the mean values of sensitivity, slope and aspect included in the landslide's perimeter (see Fig. 6A).

Landslide ID	Sensitivity	Sensitivity (asc)	Sensitivity (desc)	Slope mean (°)	Aspect mean (°)
1	0.81	0.16	0.81	33	317
2	0.57	0.09	0.57	22	219
3	0.27	0.17	0.22	26	183
4	0.51	0.15	0.49	33	199
5	0.56	0.09	0.56	19	223

orbits are consistently low (0.09–0.17), whereas descending acquisitions show higher sensitivity values (0.22–0.81).

Only landslide ID3 shows a relatively low sensitivity value, although it remains above the 0.2 threshold. This reduced sensitivity results from the interplay between slope aspect and the Sentinel-1 radar LOS geometry, which attenuates the signal in ascending acquisitions. Consequently, ascending-orbit datasets were excluded from subsequent analyses because their reduced sensitivity limits the detection of slope-parallel deformation.

Fig. 9 provides an overview of landslide displacements from descending-orbit time series with temporal coherence >0.5. Median displacement and IQR are shown for each mapped landslide after applying a 60-day rolling mean to reduce short-term noise and highlight long-term trends. The lower-right panels show the annual mean LOS velocity of each PS.

Seismic shaking conditions affecting the study area were analyzed using shake maps provided by the Seismological Laboratory of the University of Athens. Earthquakes occurring between 2018 and 2023 with moment magnitude $M_w \geq 4.5$ were considered. For each event, Peak Ground Acceleration (PGA) values and hypocentral depths were extracted at the locations of the mapped landslides (Table 2).

The analyzed seismic sequence encompasses magnitudes ranging from 4.5 to 5.2 M_w, with relatively shallow hypocentral depths between 4 and 9 km. Extracted PGA values exhibit significant spatial variability across the landslide's sites, reflecting both the source characteristics of each earthquake, and local site conditions. While PGA values typically remained below 3%g, the 4.8 M_w event of 12 January 2021, with a hypocentral depth of 4 km, generated markedly higher ground accelerations. During this event, PGA reached 9.75%g at landslide ID3 and exceeded 5%g at several other investigated sites. These data indicate that, despite the moderate regional seismicity during the analyzed period, shallow events may produce localized ground accelerations of significant amplitude at landslide sites.

Fig. 10 summarizes the temporal evolution of landslides between 2019 and 2023 by combining InSAR-derived LOS velocities from the descending orbit with rainfall and seismic activity. The 60-day cumulative precipitation exhibits a strong seasonal signal, with recurring peaks that are relatively consistent in both magnitude and timing across years. These peaks typically occur during late winter (December–February), reaching values between 250 and 350 mm.

Earthquakes with $M_w \geq 3$ are presented as a cumulative sum over 60-day periods. The seismic record during the five-year analysis period is characterized by persistent background activity, interrupted by a pronounced increase in seismicity between late 2020 and early 2021. During this interval, both the cumulative number of events and the frequency of larger magnitudes ($M_w \geq 4.5$) increase sharply, reflecting a concentrated seismic sequence rather than a sustained trend.

The LOS velocity was estimated using a 60-day moving window approach, where a linear regression was fitted to the displacement time series within each window. The resulting slope was converted into annualized velocity (mm/year). The median velocity among the retained PS was then calculated for each acquisition date, with the IQR used to represent the spatial variability of deformation.

The mapped landslides exhibit different deformation behaviors over the five-year investigation period. The most pronounced velocity fluctuations are observed for landslide ID2, whereas landslide ID4 shows a more regular and seasonal deformation pattern characterized by a quasi-

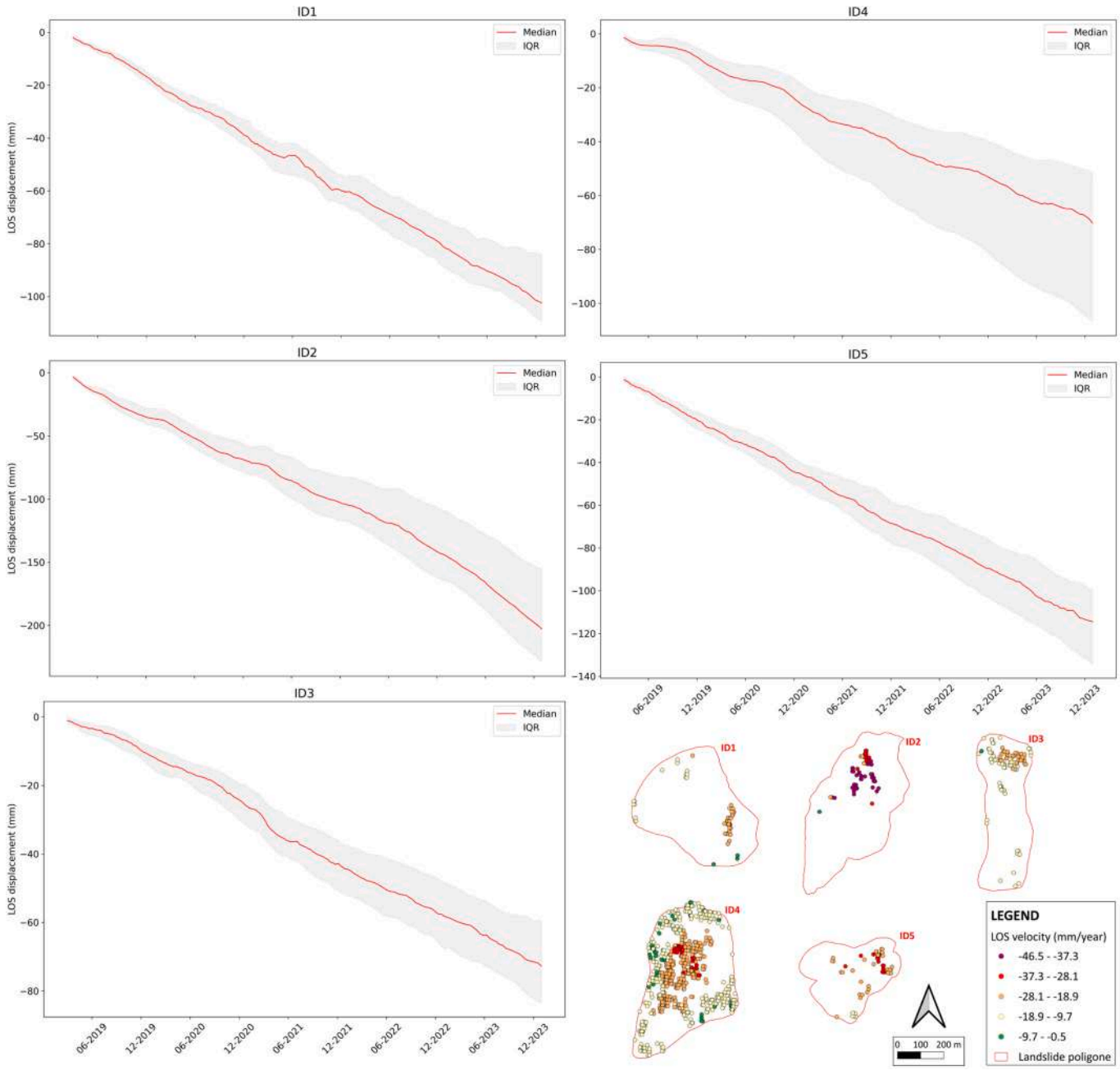

Fig. 9. Median displacement time-series (2019–2023) of the five landslides mapped. Bottom right maps indicate the PS mean velocity (mm/year) derived from EGMS attribute table.

Table 2
Major earthquake in the area between 2019 and 2023. The PGA (%g) is reported for each mapped landslide.

Event date	M_w	Depth (km)	PGA ID1	PGA ID2	PGA ID3	PGA ID4	PGA ID5
30/03/2019	5.2	7	1.64	1.43	1.43	1.70	2.17
23/12/2020	4.5	9	1.02	1.48	1.48	0.88	0.75
12/01/2021	4.8	4	5.36	6.41	9.75	6.41	3.60
17/02/2021	4.9	6	2.32	3.64	3.76	2.49	1.78

sinusoidal trend. A general increase in signal noise is observed during the final two years of the observation period (2022−2023) in most of the time series. To explore correlations between different forcings, the k-means clustering results—shown as shaded grey bands—partition the observation period into discrete temporal regimes. Cluster 1 corresponds to the seismic sequence from late 2020 to early 2021, marked by dozens of earthquakes with $M_w \geq 3$ and three major events with $M_w \geq 4.5$. Cluster 2 coincides with heavy rainfall period, where peaks in the 60-day cumulative precipitation aligns with negative high-transient LOS velocity peaks, except in the landslide ID2 plot. Cluster 3 identifies period with intermediate behavior, while Cluster 4 reflects kinematic quiescence, with low or decelerating LOS velocities, minimal rainfall, and low seismic activity, suggesting relatively stable slope conditions.

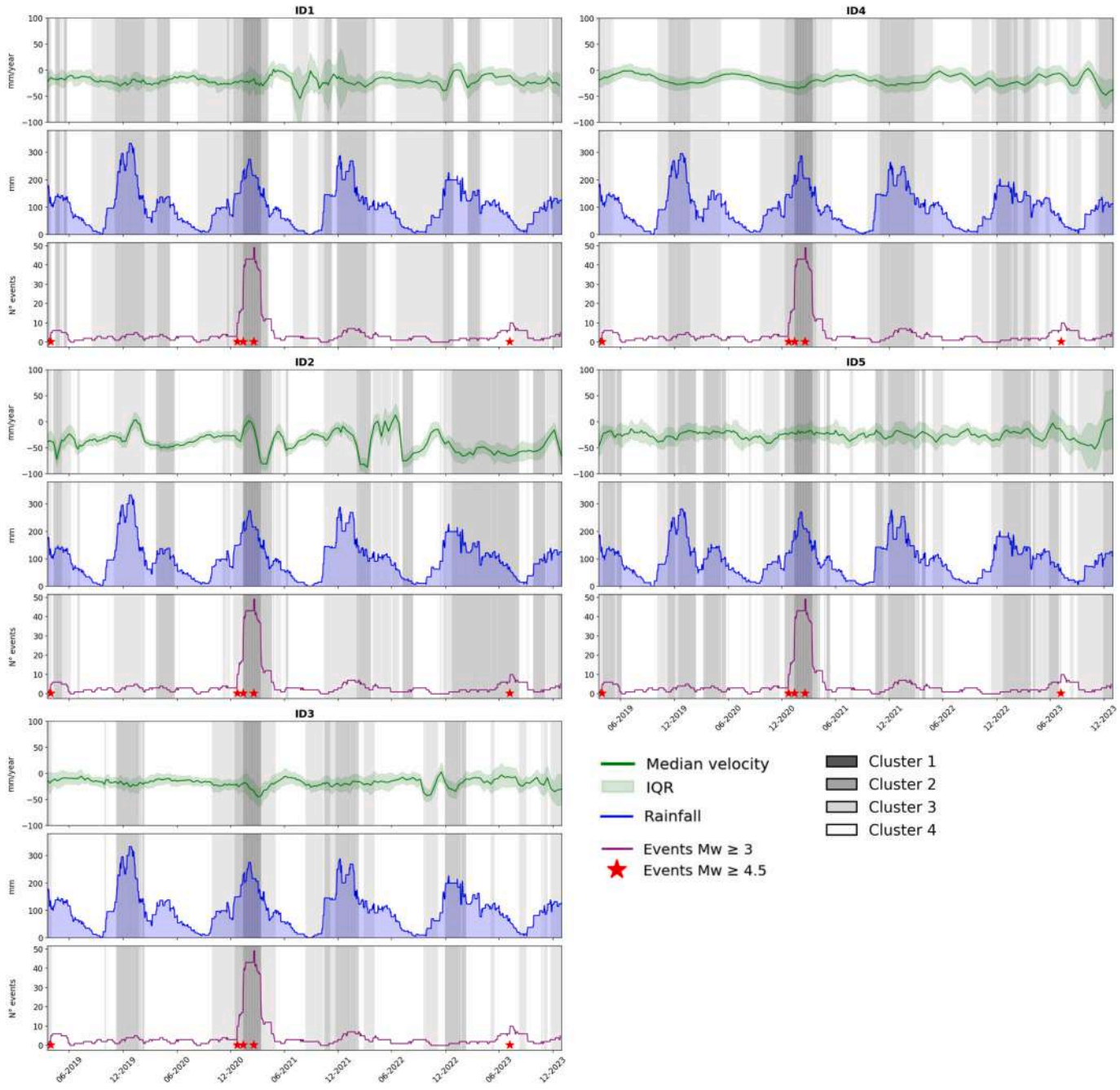

Fig. 10. Temporal comparison of LOS velocity (mm/year; median and IQR derived from a 60-day moving linear regression of descending-orbit time series), 60-day cumulative rainfall, and seismic activity (cumulative number of Mw $\geq$ 3 events over 60 days and individual Mw $\geq$ 4.5 events). Grey shaded bands indicate temporal regimes identified through k-means clustering. Panels ID1–ID5 show the deformation response of individual landslides to external forcing during the 2019–2023 observation period.

5. Discussion

In the western sector of the Corinth Rift (Fig. 1B), active landslides were initially identified using a k-means time-series analysis of Sentinel-1 InSAR data. This methodology can be applied to a wide range of active tectonic settings, facilitating the discrimination of landslide-related deformation from other transient ground movements. The PS belonging to Cluster 4, interpreted as landslide-related based on their displacement behavior (Fig. 5B and D), were successfully validated through subsequent geomorphological field investigations (Figs. 6).

Field surveys and comparison with the geological map (Figs. 2 and 7) revealed a spatial association between all mapped landslides and major tectonic contacts, suggesting potential structural control on slope movements. The systematic correspondence between landslide occurrence and tectonic structures indicates that fault-related damage zones likely exert control on slope failure by promoting bedrock weakening and enhancing fracture-controlled permeability. The study area is crossed by a major thrust fault along which landslides ID1, ID2, and ID3 are located. This thrust juxtaposes siliciclastic units against limestone formations. The ID2 landslides (also referred to "Marathias landslide" by Gallousi and Koukouvelas, 2007) is situated at the intersection between the main thrust and the Marathias fault system, which cuts across the thrust in correspondence with the landslide. Notably, the main crown of landslide ID2 displays an L-shaped geometry (Figs. 7B and 8A): the

east–west-trending segment is parallel to the Marathias fault, whereas the north–south-trending segment is parallel to the thrust. Such geometry strongly suggests structural control on landslide development. Along the landslide ID3 crown, a well-defined fault trace was identified and mapped (Figs. 7C and 8E), further supporting the influence of tectonic structures on slope evolution. In this area as well, an intersection between a fault and the thrust is observed. Landslide ID4 exhibits a more complex morphology (Fig. 8B). Field evidence of thrust-related deformation observed in the outcropping bedrock at the landslide toe further supports a relationship with the second major thrust crossing the study area. Finally, the ID5 landslide complex is also developed along a clear tectonic-stratigraphic contact between siliciclastic and limestone units (Fig. 7E).

In general, the bedrock observed in the study area exhibits a high degree of weathering, deformation, and fracturing in proximity to fault zones, representing a significant predisposing factor for slope failure. Such conditions likely reduce rock mass strength while simultaneously increasing water infiltration, thereby enhancing susceptibility to slope failures. These observations are consistent with previous studies on slope instability in the Gulf of Corinth (e.g., Gallousi and Koukouvelas, 2007; Koukis et al., 2009; Sabatakakis et al., 2015). The crowns of all mapped landslides are located within thin-bedded to fine-bedded limestone units, suggesting lithological control on landslide occurrence, consistent with the findings of Bathrellos et al. (2024) in the northwestern Peloponnese. Furthermore, the role of karst processes characterizing this geological formation (Fig. 8D) cannot be excluded and may contribute to slope instability through enhanced rock mass heterogeneity and secondary porosity, as suggested by field evidence.

The geological and geomorphological constraints discussed above provide an important framework for interpreting the deformation patterns observed through satellite monitoring. In terms of cumulative displacement (Fig. 9), the ID1 and ID5 landslides show predominantly linear behavior, whereas ID4 exhibits quasi-linear temporal dynamics characterized by a seasonal component. The ID2 time series displays a linear trend until summer 2022, when a clear acceleration phase occurred. ID3 exhibits the most heterogeneous behavior, including a pronounced acceleration phase during winter 2020–2021.

The mapped slope failures exhibit markedly different deformation responses to rainfall and seismic activity, indicating that external forcings interact with landslide-specific internal conditions rather than producing uniform deformation across the study area (Fig. 10). ID1 shows limited deformation mainly controlled by cumulative rainfall, with no clear acceleration directly attributable to the 2020–2021 seismic sequence. In contrast, ID2 exhibits the most complex response, with marked velocity variability and a delayed peak occurring approximately two months after intense rainfall and seismic activity, suggesting a time-lagged, memory-controlled response. In this case, seismic shaking may have acted as a preconditioning factor, enhancing the subsequent hydrological response, possibly also modulated by karst groundwater circulation. By comparison, ID3 shows moderate velocity peaks during the January 2021 event despite experiencing the highest PGA, whereas ID4 displays predominantly rainfall-driven, quasi-seasonal deformation patterns with no evident delayed seismic effects. ID5 shows no relevant correlation between velocity and external forcings.

However, the specific contribution of seismic shaking remains difficult to quantify during the study period. The most intense seismic sequence coincided with peak 60-day cumulative rainfall during the wet season, limiting the separation of seismic and hydrological effects. Therefore, the available dataset does not allow a direct attribution of acceleration phases to seismic forcing alone.

Overall, the results indicate that rainfall represents the primary triggering factor controlling short-term landslide deformation, whereas tectonic structures and lithological characteristics act as long-term predisposing factors governing slope susceptibility. Seismic shaking appears to play a secondary and site-specific role, mainly through preconditioning mechanisms that may enhance the subsequent hydrological response.

6. Conclusion

This study integrates InSAR time series, geomorphological mapping, and analysis of external forcing to investigate deep-seated landslides in the western Gulf of Corinth. The results show that landslide deformation is systematically concentrated along major tectonic structures and lithological boundaries, confirming the primary role of tectono-lithological conditioning factors in controlling slope instability at the regional scale.

A key outcome of this work is the successful discrimination of landslide-related deformation from tectonic-related ground motion in an actively deforming region through InSAR time-series clustering. This highlights the need for careful interpretation of satellite-based displacement data in tectonically active regions, where multiple sources of ground motion may coexist.

Temporal analysis indicates that rainfall represents the dominant short-term driver of landslide activity, while seismic shaking acts as a secondary, site-dependent factor that may modulate slope response and contribute to delayed acceleration phases. However, the influence of seismic forcing is strongly conditioned by local geological and hydrological properties, leading to heterogeneous responses among landslides.

Overall, the study emphasizes that reliable characterization of landslide dynamics in complex tectonic settings requires the integration of remote sensing, field-based geomorphological analyses, and the assessment of external forcing. Such an interdisciplinary approach is essential to disentangle overlapping deformation processes and improve the understanding of slope behavior in tectonically active areas.

CRediT authorship contribution statement

Francesco Seitone: Writing – original draft, Methodology, Investigation, Formal analysis, Data curation, Conceptualization. **Michele Licata:** Writing – review & editing, Visualization, Validation, Methodology, Investigation, Data curation. **Konstantinos Tsanakas:** Writing – review & editing, Supervision. **Efthimios Karymbalis:** Writing – review & editing, Validation, Supervision. **Giandomenico Fubelli:** Writing – review & editing, Validation, Supervision, Project administration, Conceptualization.

Declaration of competing interest

The authors declare that they have no known competing financial interests or personal relationships that could have appeared to influence the work reported in this paper.

Data availability

Data will be made available on request.

References

Armijo, R., Meyer, B., King, G.C.P., Rigo, A., Papanastassiou, D., 1996. Quaternary evolution of the Corinth Rift and its implications for the late Cenozoic evolution of the Aegean. Geophys. J. Int. 126, 11–53. https://doi.org/10.1111/j.1365-246X.1996.tb05264.x.

Armijo, R., Meyer, B., Hubert, A., Barka, A., 1999. Westward propagation of the North Anatolian fault into the northern Aegean: timing and kinematics. Geology 27, 267–270. https://doi.org/10.1130/0091-7613.

Athanassas, C.D., Papanikolaou, D.I., Falkowski, S., Papanikolaou, I.D., Ntokos, D., 2021. Thermotectonic constraints on the geodynamic evolution of the Pindos fold-and-thrust-belt by low-temperature (U–Th)/He thermochronometry. Geol. J. 56, 5311–5328. https://doi.org/10.1002/gj.4240.

Avallone, A., Briole, P., Agatza-Balodimou, A.M., Billiris, H., Charade, O., Mitsakaki, C., Nercessian, A., Papazissi, K., Paradissis, D., Veis, G., 2004. Analysis of eleven years of deformation measured by GPS in the Corinth rift laboratory area. Compt. Rendus Geosci. 336, 301–311. https://doi.org/10.1016/j.crte.2003.12.007.

Bathrellos, G.D., Koukouvelas, I.K., Skilodimou, H.D., Nikolakopoulos, K.G., Vgenopoulos, A.-L., 2024. Landslide causative factors evaluation using GIS in the

tectonically active Glafkos River area, northwestern Peloponnese, Greece. Geomorphology 461, 109285. https://doi.org/10.1016/j.geomorph.2024.109285.
Beckers, A., Hubert-Ferrari, A., Beck, C., Bodeux, S., Tripsanas, E., Sakellariou, D., De Batist, M., 2015. Active faulting at the western tip of the Gulf of Corinth, Greece, from high-resolution seismic data. Mar. Geol. 360, 55–69.
Bernard, P., Briole, P., Meyer, B., Gomez, J., Tiberi, C., Berge, C., Cattin, R., Hatzfeld, D., Lachet, C., Lebrun, B., 1997. The Ms 6.2, June 15, 1995, Aigion earthquake (Greece): evidence for low-angle normal faulting in the Corinth Rift. J. Seismol. 1, 131–150. https://doi.org/10.1023/A:1009795618839.
Bernard, P., Lyon-Caen, H., Briole, P., Deschamps, A., Boudin, F., Makropoulos, K., et al., 2006. Seismicity, deformation and seismic hazard in the western rift of Corinth: New insights from the Corinth Rift Laboratory (CRL). Tectonophysics 426 (1–2), 7–30. https://doi.org/10.1016/j.tecto.2006.02.012.
Bianchini, S., Herrera, G., Mateos, R.M., Notti, D., Garcia, I., Mora, O., Moretti, S., 2013. Landslide activity maps generation by means of persistent scatterer interferometry. Remote Sens. 5 (12), 6198–6222. https://doi.org/10.3390/rs5126198.
Bontemps, N., Lacroix, P., Larose, E., Jara, J., Taipe, E., 2020. Rain and small earthquakes maintain a slow-moving landslide in a persistent critical state. Nat. Commun. 11 (1), 780. https://doi.org/10.1038/s41467-020-14445-3.
Briole, P., Rigo, A., Lyon-Caen, H., Ruegg, J.C., Papazissi, K., Mitsakaki, C., Balodimou, A., Veis, G., Hatzfeld, D., Deschamps, A., 2000. Active deformation of the Corinth rift, Greece: results from repeated Global Positioning System surveys between 1990 and 1995. J. Geophys. Res. 105 (B11), 25605–25625. https://doi.org/10.1029/2000JB900148.
Briole, P., Ganas, A., Elias, P., Dimitrov, D., 2021. The GPS velocity field of the Aegean: new observations, contribution of the earthquakes, crustal blocks model. Geophys. J. Int. 226, 468–492.
Carlini, M., Chelli, A., Vescovi, P., Artoni, A., Clemenzi, L., Tellini, C., Torelli, L., 2016. Tectonic control on the development and distribution of large landslides in the Northern Apennines (Italy). Geomorphology 253, 425–437. https://doi.org/10.1016/j.geomorph.2015.10.028.
Crosetto, M., Solari, L., Mróz, M., Balasis-Levinsen, J., Casagli, N., Frei, M., Oyen, A., Moldestad, D.A., Bateson, L., Guerrieri, L., Comerci, V., Andersen, H.S., 2020. The evolution of wide-area DInSAR: from regional and national services to the European ground motion service. Remote Sens. 12 (12), 2043. https://doi.org/10.3390/rs12122043.
Davies, D.L., Bouldin, D.W., 1979. A Cluster Separation Measure. IEEE Trans. Pattern Anal. Mach. Intell. PAMI-1 (2), 224–227. https://doi.org/10.1109/TPAMI.1979.4766909.
Doutsos, T., Piper, D.J.W., 1990. Listric faulting, sedimentation, and morphological evolution of the Quaternary eastern Corinth Rift, Greece: first stages of continental rifting. Bull. Geol. Soc. Am. 102, 812–829.
Fernández-Blanco, D., De Gelder, G., Lacassin, R., Armijo, R., 2019. A new crustal fault formed the modern Corinth Rift. Earth Sci. Rev. 199, 102919. https://doi.org/10.1016/j.earscirev.2019.102919.
Festa, D., Novellino, A., Hussain, E., Bateson, L., Casagli, N., Confuorto, P., Del Soldato, M., Raspini, F., 2023. Unsupervised detection of InSAR time series patterns based on PCA and K-means clustering. Int. J. Appl. Earth Obs. Geoinf. 118, 103276. https://doi.org/10.1016/j.jag.2023.103276.
Funk, C., Peterson, P., Landsfeld, M., Pedreros, D., Verdin, J., Shukla, S., Husak, G., Rowland, J., Harrison, L., Hoell, A., Michaelsen, J., 2015. The climate hazards InfraRed precipitation with stations—CHIRPS: a quasi-global, high-resolution precipitation dataset. Remote Sens. Environ. 166, 121–140. https://doi.org/10.1016/j.rse.2015.05.015.
Gallousi, C., Koukouvelas, I.K., 2007. Quantifying geomorphic evolution of earthquake-triggered landslides and their relation to active normal faults: an example from the Gulf of Corinth, Greece. Tectonophysics 440 (1–4), 85–104. https://doi.org/10.1016/j.tecto.2007.02.009.
Houghton, S.L., Roberts, G.P., Papanikolaou, D., McArthur, J.M., 2003. New 234U-230Th coral dates from the western Gulf of Corinth: implications for extensional tectonics. Geophys. Res. Lett. 30/19, SDE13-1–SDE13-4. https://doi.org/10.1029/2003GL018112.
Intrieri, E., Bardi, F., Fanti, R., Gigli, G., Fidolini, F., Casagli, N., Costanzo, S., Raffo, A., Di Massa, G., Capparelli, G., Versace, P., 2017. Big data managing in a landslide early warning system: experience from a ground-based interferometric radar application. Nat. Hazards Earth Syst. Sci. 17, 1713–1723. https://doi.org/10.5194/nhess-17-1713-2017.
Jaboyedoff, M., Labiouse, V., 2011. Preliminary estimation of rockfall runout zones. Nat. Hazards Earth Syst. Sci. 11, 819–828. https://doi.org/10.5194/nhess-11-819-2011.
Karymbalis, E., Ferentinou, M., Giles, P.T., 2018. Morphometric clustering of alluvial fans using self-organizing maps. Geol. Soc. Lond. Spec. Publ. 440, 45–64. https://doi.org/10.1144/SP440.7.
Kaviris, G., Millas, C., Spingos, I., Kapetanidis, V., Fountoulakis, I., Papadimitriou, P., Voulgaris, N., Makropoulos, K., 2018. Shear-wave splitting in the western Gulf of Corinth. Phys. Earth Planet. Inter. 282, 60–76. https://doi.org/10.1016/j.pepi.2018.07.005.
Kaviris, G., Elias, P., Kapetanidis, V., Serpetsidaki, A., Karakonstantis, A., Plicka, V., De Barros, L., Sokos, E., Kassaras, I., Sakkas, V., 2021. The Western Gulf of Corinth 2020–2021 seismic crisis. Seism. Rec. 1, 85–95. https://doi.org/10.1785/0320210021.
Kaviris, G., Zymvragakis, A., Bonatis, P., Kapetanidis, V., Voulgaris, N., 2022. Probabilistic and scenario-based seismic hazard assessment on the Western Gulf of Corinth (Central Greece). Appl. Sci. 12, 11152. https://doi.org/10.3390/app122111152.
Keefer, D.K., 1984. Landslides caused by earthquakes. Geol. Soc. Am. Bull. 95, 406–421.
Keefer, D.K., 2002. Investigating landslides caused by earthquakes. Surv. Geophys. 23, 473–510. https://doi.org/10.1023/A:1021274710840.
Koukis, G., Sabatakakis, N., Ferentinou, M., Lainas, S., Alexiadou, X., Panagopoulos, A., 2009. Landslides related to fault tectonics in Corinth Gulf. Bull. Eng. Geol. Environ. 68, 215–229. https://doi.org/10.1007/s10064-008-0184-8.
Lacroix, P., Perfettini, H., Taipe, E., et al., 2014. Coseismic and postseismic motion of a landslide. Geophys. Res. Lett. 41, 6676–6680. https://doi.org/10.1002/2014GL061170.
Lacroix, P., Gavillon, T., Bouchant, C., Lavé, J., Mugnier, J.-L., Dhungel, S., Vernier, F., 2022. Post-seismic landslide motion after the Gorkha earthquake. Sci. Rep. 12, 6266. https://doi.org/10.1038/s41598-022-10016-2.
Lakhote, A., Chan, Y.-C., Lu, C.-Y., Kumar, G., Sun, C.-W., 2025. Monitoring slow-moving landslide using PSI. Landslides 22, 1677–1692. https://doi.org/10.1007/s10346-024-02453-z.
Lambotte, S., Lyon-Caen, H., Bernard, P., Deschamps, A., Patau, G., Nercessian, A., Pacchiani, F., Bourouis, S., Drilleau, M., Adamova, P., 2014. Reassessment of the rifting process in the Western Corinth Rift from relocated seismicity. Geophys. J. Int. 197, 1822–1844.
Li, M., Wu, H., Yang, M., Huang, C., Tang, B.-H., 2023. Trend classification of InSAR displacement time series using SAE–CNN. Remote Sens. 16 (1), 54. https://doi.org/10.3390/rs16010054.
MacQueen, J., 1967. Some methods for classification and analysis of multivariate observations. Proceedings of the Fifth Berkeley Symposium on Mathematical Statistics and Probability Vol. 1, 281–297.
Makropoulos, K., Kaviris, G., Kouskouna, V., 2012. An updated and extended earthquake catalogue for Greece and adjacent areas since 1900. Nat. Hazards Earth Syst. Sci. 12, 1425–1430. https://doi.org/10.5194/nhess-12-1425-2012.
Mantovani, M., Devoto, S., Piacentini, D., Prampolini, M., Soldati, M., Pasuto, A., 2016. Advanced SAR interferometric analysis to support geomorphological interpretation of slow-moving coastal landslides (Malta, Mediterranean Sea). Remote Sens. 8 (6), 443. https://doi.org/10.3390/rs8060443.
Martino, S., 2016. Earthquake-induced reactivation of landslides: Recent advances and future perspectives. In: D'Amico, S. (Ed.), Earthquakes and Their Impact on Society. Springer International Publishing, pp. 291–322. https://doi.org/10.1007/978-3-319-21753-6_10.
Martino, S., Fiorucci, M., Marmoni, G.M., Casaburi, L., Antonielli, B., Mazzanti, P., 2022. Increase in landslide activity after a low-magnitude earthquake as inferred from DInSAR interferometry. Sci. Rep. 12 (1), 2686. https://doi.org/10.1038/s41598-022-06508-w.
Mavroulis, S., Sarantopoulou, A., Lekkas, E., 2025. Earthquake-triggered landslides in Greece from antiquity to the present: temporal, spatial and statistical GIS-based analysis. Land 14 (2), 307. https://doi.org/10.3390/land14020307.
McColl, S.T., Cook, S.J., 2024. A universal size classification system for landslides. Landslides 21, 111–120. https://doi.org/10.1007/s10346-023-02131-6.
McNeil, L.C., Collier, R.E.L., De Martini, P.M., Pantosti, D., D'Adezio, G., 2005. Recent history of the Eastern Eliki fault, Gulf of Corinth: geomorphology, palaeoseismology and impact on palaeoenvironments. Geophys. J. Int. 161, 154–166. https://doi.org/10.1111/j.1365-246X.2005.02559.x.
Micu, M., Micu, D., Havenith, H.-B., 2023. Earthquake-induced landslide hazard assessment in the Vrancea Seismic Region (Eastern Carpathians, Romania): Constraints and perspectives. Geomorphology 427, 108635. https://doi.org/10.1016/j.geomorph.2023.108635.
van Natijne, A.L., Bogaard, T.A., van Leijen, F.J., Hanssen, R.F., Lindenbergh, R.C., 2022. InSAR landslide sensitivity index. J. Appl. Geod. 111, 102829.
Newmark, N.M., 1965. Effects of earthquakes on dams and embankments. Geotechnique 15 (2), 139–159.
Nomikou, P., Alexandri, M., Lykousis, V., Sakellariou, D., Ballas, D., 2011. Swath bathymetry and morphological slope analysis of the Corinth Gulf. In: Proceedings of the 2nd INQUA-IGCP-567 International Workshop on Active Tectonics, Earthquake Geology, Archaeology and Engineering, pp. 155–158.
Notti, D., Herrera, G., Bianchini, S., Meisina, C., García-Davalillo, J.C., Zucca, F., 2014. A methodology for improving landslide PSI data analysis. Int. J. Remote Sens. 35 (6), 2186–2214. https://doi.org/10.1080/01431161.2014.889864.
Palyvos, N., Pantosti, D., De Martini, P.M., Lemeille, F., Sorel, D., Pavlopoulos, K., 2005. The Aigion-Neos Erineos coastal normal fault system (western Corinth Rift, Greece): geomorphological signature, recent earthquake history, and evolution. J. Geophys. Res. 110, B09302. https://doi.org/10.1029/2004JB003165.
Palyvos, N., Lemeille, F., Sorel, D., Pantosti, D., Pavlopoulos, K., 2008. Geomorphic and biological indicators of paleoseismicity and Holocene uplift rate at a coastal normal fault footwall (western Corinth Gulf, Greece). Geomorphology 96, 16–38. https://doi.org/10.1016/j.geomorph.2007.07.010.
Papanikolaou, D.I., 2021. The Geology of Greece. Springer. https://doi.org/10.1007/978-3-030-60731-9.
Paraschoudis, B., 1977. Geological map of Greece, Amygdalea sheet (1:50,000). Institute of Geology and Mineral Exploration (IGME).
Parkash, S., 2020. Training Module on Comprehensive Landslides Risk Management. National Institute of Disaster Management, p. 335.
Piacentini, D., Devoto, S., Mantovani, M., Pasuto, A., Prampolini, M., Soldati, M., 2015. Landslide susceptibility modeling assisted by Persistent Scatterers Interferometry (PSI): an example from the northwestern coast of Malta. Nat. Hazards 78, 681–697. https://doi.org/10.1007/s11069-015-1740-8.
Pilade, F., Licata, M., Vasiliev, I., Fubelli, G., Gennari, R., 2025. The GEMMA toolbox: a user-friendly software for multivariate analysis. Comput. Geosci. 199, 105914. https://doi.org/10.1016/j.cageo.2025.105914.

Poggi, F., Nardini, O., Fiaschi, S., Montalti, R., Intrieri, E., Raspini, F., 2025. Multi-sensor satellite analysis for landslide characterization: a case of study from Baipaza, Tajikistan. Remote Sens. 17 (12), 2003. https://doi.org/10.3390/rs17122003.
Reilinger, R., McClusky, S., Paradissis, D., Ergintav, S., Vernant, P., 2009. Geodetic constraints on the tectonic evolution of the Aegean region. Tectonophysics 488, 22–30. https://doi.org/10.1016/j.tecto.2009.05.027.
Rigo, A., Lyon-Caen, H., Armijo, R., Deschamps, A., Hatzfeld, D., Makropoulos, K., Papadimitriou, P., Kassaras, I., 1996. A microseismic study in the western part of the Gulf of Corinth (Greece): Implications for large-scale normal faulting mechanisms. Geophys. J. Int. 126, 663–688.
Rossi, S., Tsanakas, K., Bucci, M.G., Sakellariou, D., Soldati, M., Karymbalis, E., 2026. Geomorphological mapping of the Gulf of Corinth. J. Maps. https://doi.org/10.1080/17445647.2026.2621506.
Rousseeuw, P.J., 1987. Silhouettes: a graphical aid to the interpretation and validation of cluster analysis. J. Comput. Appl. Math. 20, 53–65. https://doi.org/10.1016/0377-0427(87)90125-7.
Rygus, M., Novellino, A., Hussain, E., Syafiudin, F., Andreas, H., Meisina, C., 2023. Clustering InSAR time series in Bandung basin. Remote Sens. 15, 3776. https://doi.org/10.3390/rs15153776.
Sabatakakis, N., Tsiambaos, G., Rondoyanni, T., Papanakli, S., Kavoura, K., 2015. Deep-seated structurally controlled landslides of Corinth Gulf rift zone, Greece: the case of Panagopoula landslide. In: Proceedings of the ISRM Congress, pp. 1–8.
Skourlis, K., Doutsos, T., 2003. Inversion tectonics of the Pindos belt. Int. J. Earth Sci. 92, 891–903.
Sokos, E., Zahradník, J., Kiratzi, A., et al., 2012. Efpalio earthquake sequence. Tectonophysics 530–531, 299–309.
Soldati, M., 2013. Deep-seated gravitational slope deformation. In: Bobrowsky, P.T. (Ed.), Encyclopedia of Natural Hazards. Springer, Dordrecht, pp. 151–155.
Song, C., Yu, C., Li, Z., Utili, S., Frattini, P., Crosta, G., Peng, J., 2022. Earthquake-accelerated landslides in Italy. Nat. Commun. 13, 7278.
Taylor, B., Weiss, J.R., Goodliffe, A.M., Sachpazi, M., Laigle, M., Hirn, A., 2011. The structures, stratigraphy and evolution of the Gulf of Corinth rift, Greece: structures, stratigraphy and evolution of GoC. Geophys. J. Int. 185, 1189–1219.
Taymaz, T., Jackson, J., McKenzie, D., 1991. Active tectonics of the north and central Aegean Sea. Geophys. J. Int. 106, 433–490.
Toločka, A., 2025. Global distribution of deep-seated gravitational deformations. Nat. Hazards 121, 16149–16183.
Torre, D., Galve, J.P., Reyes-Carmona, C., et al., 2024. InSAR and geomorphology integration. Landslides 21, 1273–1292.
Tsanakas, K., Karymbalis, E., Griva, D., et al., 2025. Geomorphology of Greece. J. Maps 21 (1).
Tsoflias, P., Loftus, D.L., 1971. Geological Map of Greece: Nafpaktos Sheet. IGME.
Varnes, D.J., 1978. Slope movement types and processes. In: Landslides. National Academy of Sciences, pp. 11–33.
Zahradník, J., Aissaoui, E.M., Bernard, P., Briole, P., Bufféral, S., De Barros, L., 2022. Corinth rift earthquake. J. Geophys. Res. Solid Earth 127, e2022JB024221.

Website references

1 European Ground Motion Service. Available online: https://egms.land.copernicus.eu/ (accessed 14 May 2026).
2 National Kapodistrian University of Athens (NKUA) Seismological Laboratory. Available online: http://geophysics.geol.uoa.gr/ (accessed 14 May 2026).
3 CHIRPS. Rainfall Estimates from Rain Gauge and Satellite Observations. Available online: https://www.chc.ucsb.edu/data/chirps (accessed 14 May 2026).